

Three-dimensional forward scattering particle image velocimetry applied to a microscopic field-of-view

B. Ovryn

Abstract We have completed a model to predict the three-dimensional position of a spherical particle from the image formed by a high numerical aperture microscope. Although this information may be exploited in a number of different ways, we are particularly interested in determining the three components of velocity for seed particles following a flow. The basis of the model is to use Mie theory to determine the complete electromagnetic field scattered by a spherical particle and then to propagate the scattered field across the interface between sample and air and then through a high aperture microscope and ultimately to a detector.

1 Introduction

The development of techniques to study flow in a microscopic (i.e., sub-millimeter) field-of-view (FOV) is an active area of research. Techniques for tracking a particle in two dimensions have been developed to measure the microrheology of complex fluids (Gittes et al. 1997; Mason et al. 1997), the hydrodynamic interaction between colloidal particles (Kepler and Fraden 1994; Meiners and Quake 1999) and their interaction with confining walls (Dufresne et al. 2000), and the motion of molecular motors probed with optical traps (Visser and Block 1998). In the latter category, one-dimensional displacements have been determined with sub-nanometer accuracy by measuring the change in polarization of two initially, orthogonally polarized waves as they propagate through a transparent sphere and then recombine at a quadrant detector (Denk and Webb 1990; Svoboda et al. 1993).

Recently, Santiago et al. (1998) have used sub-micron particles to demonstrate that conventional particle

imaging velocimetry (PIV) techniques (Willert and Gharib 1991; Wernet and Pline 1993) may be applied to the measurement of two-dimensional velocity profiles in a microscopic FOV. Although whole-field PIV techniques including holographic PIV (Meng and Hussain 1991; Barnhart et al. 1994; Fabry 1998) and stereo imaging (Prasad and Adrian 1993; Wernet 1996) have been developed to measure three-dimensional flow, these methods have not yet been extended to a microscopic FOV (Hinsch 1995). Alternatively, whole-field video microscopy techniques (Crocker and Grier 1996), which rely on the narrow “depth-of-focus” of a lens, have been developed to determine the position of a particle along the line sight; this direction is usually referred to as the optical axis (OA). Point-wise techniques, such as color Doppler optical coherence tomography (OCT), have also been used to measure three-dimensional flow in a microscopic FOV (Wang et al. 1997; Yazdanfar et al. 1997; Imai and Tanaka 1999) and in vivo applications have been demonstrated.

In contrast with previous approaches which determine velocities without resolving the detailed structure of the scattering, we have developed a technique which relies on the resolution of the detailed structure of the scattering from spherical particles in order to determine the position along the optical axis of the imaging system. When combined with tracking of the transverse position of the particle’s centroid, this technique may be used to determine the three-dimensional position of a particle as a function of time. We have called this technique “coherent forward scattering particle image velocimetry (CFSPIV) (Ovryn and Hovenac 1994; Ovryn et al. 1995; Khaydarov and Ovryn 1996; Ovryn and Khaydarov 1997; Ovryn et al. 1998; Izen and Ovryn 1999). Because the illuminating source is only partially coherent, we use the term “FSPIV” (Izen and Ovryn 1998).

2 Optical model used to predict the scattering

The basis of the model (Ovryn and Izen 2000) is to use Mie calculations to determine the electromagnetic field scattered by a spherical particle and then to propagate the scattered field across the transparent wall of the flow cell, through a high numerical aperture microscope objective and ultimately to a detector plane (Fig. 1). Although we have called the technique FSPIV in order to emphasize the predominate forward scattering, scattered light is actually collected in a cone (centered on the optical axis) which is determined by the numerical aperture (NA) of the lens; for

B. Ovryn
Department of Biomedical Engineering
Case Western Reserve University
Wickenden Building, 10900 Euclid Avenue
Cleveland, Ohio 44106-7207, USA

This work was supported by the Microgravity Research Division, NASA, partially under grant NAG3-1391. The author would like to acknowledge the contributions of J. D. Khaydarov (Continuum, Inc.) while he was a Research Associate with the Ohio Aerospace Institute and S. H. Izen, Department of Mathematics, Case Western Reserve University, to the development of the model. Stimulating discussions with K. Das (Alcon Labs, Inc.) while he was a Resident Graduate Student at NASA are also acknowledged. Additionally, the author acknowledges K. Hallinan, Department of Mechanical Engineering, University of Dayton, for providing demanding applications for the technique.

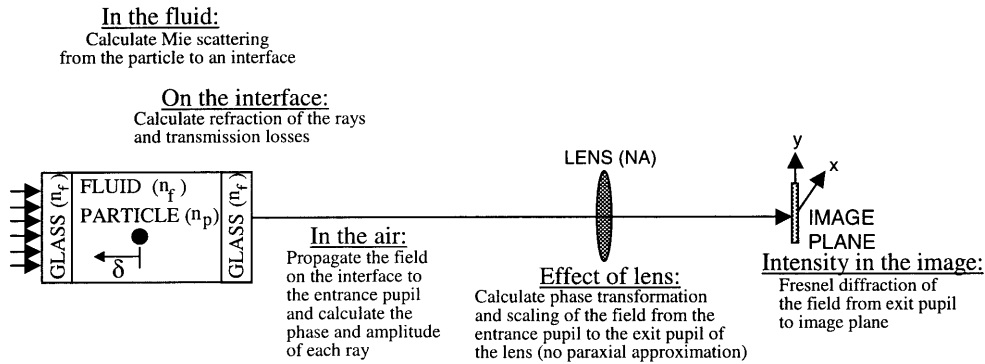


Fig. 1. Model for predicting the axial position, δ , of a spherical particle measured with respect to the fixed focus of the lens

a high NA objective lens, the angular extent of this cone is significant. The model is directly applicable to spherical particles of arbitrary size in a homogeneous medium. As illustrated in Fig. 1, the model essentially has the following steps: (1) using near-field Mie calculations, determine the vector electromagnetic fields on the fluid side of the glass-air interface (it is assumed that the glass is indexed matched to the fluid so that there is only one interface); (2) adopt a ray picture and determine the effect of refraction and transmission losses caused by the interface; (3) determine the phase change and scaling of each bundle of rays as it propagates from the interface to the entrance pupil of the lens; (4) calculate the polarization rotation, phase transformation and scaling of the fields caused by the high numerical aperture microscope objective; (5) perform a two-dimensional Fresnel diffraction integral of the superposed incident and scattered fields from the exit pupil to the image plane; and (6) evaluate the Poynting vector and calculate the image which would be produced on an array detector. Corresponding to the model, we have developed a computer code, which is used to calculate the intensity for any value of the parameter δ (Fig. 1). In addition to the parameter δ , the computer code requires initial estimates for the following parameters: (1) the radius of the particle; (2) the refractive index of the particle and the fluid; (3) the wavelength of the illumination in the fluid; (4) the distance of the particle to the interface; (5) the focal length of the lens; (6) the distance from the tube lens to the intermediate image; and (7) the numerical aperture of the objective. The details of each of these steps, including a determination of the errors associated with the usual far-field approximations, may be found in Ovrzyn and Izen (2000).

3 Scattering regimes

Although useful texts have been written which describe Mie's exact solution for the electromagnetic fields scattered by a sphere from plane wave illumination (van de Hulst 1981; Boren and Huffman 1983; Barber and Hill 1990), a brief review is merited because it will establish a notation and help the reader to interpret the data which are acquired using FSPIV. When a plane wave is incident upon a transparent sphere, it may be diffracted, transmitted, absorbed and reflected; the relevant importance of each of these contributions to the scattered wavefront depends upon the radius of the sphere, a , and the ratio of its index of refraction, n_p , to that of the fluid, n_f . For example, Fig. 2 shows the transmission caustic formed by refraction of the incident rays as they transverse a sphere (centered at the point (0,0)) for two different ratios, $m = n_p/n_f$. The values of the radius of the sphere and index of refraction ratio in Fig. 2a, 3.5 μm and 1.06, respectively, correspond to the data which will be presented in Sects. 4 and 5. It may be observed from Fig. 2 that the transmitted rays form a caustic at a distance, z , beyond the sphere which is given by

$$z = \frac{ma}{2(m-1)} \quad (1)$$

In addition to the refraction caused by the sphere, rays that are transmitted through the sphere accumulate a phase relative to a reference ray which hypothetically transverses the sphere through its center (Fig. 3). The phase change of a ray which enters with an angle of incidence θ_i and which is transmitted at an angle θ_t is given by

$$\phi = \frac{2\pi a}{\lambda/n_f} (2m \cos \theta_t - 2 \cos \theta_i) \quad (2)$$

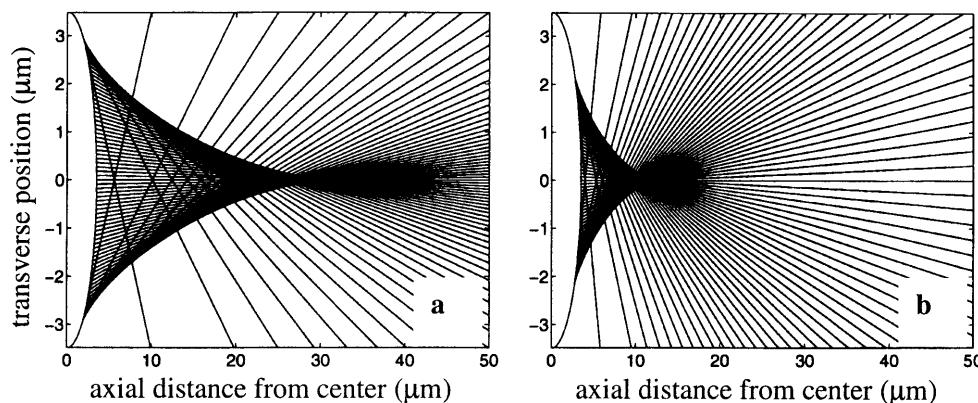


Fig. 2a, b. Transmission caustic formed by a 3.5- μm radius sphere with relative index of refraction of: a 1.06; b 1.166. The center of the sphere is located at the point (0,0)

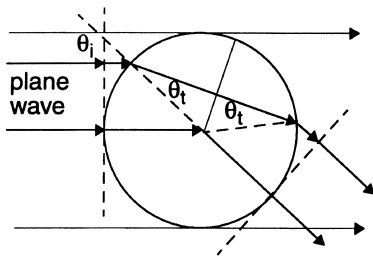


Fig. 3. Phase shift of transmitted rays relative to reference ray

The phase shift of a ray through the center of the sphere becomes

$$\rho = 2x(m - 1) \quad (3)$$

where the size parameter, x , is defined as

$$x = \frac{2\pi a}{\lambda/n_f} \quad (4)$$

Because the Mie calculations provide a rigorous prediction of the scattering for any size spherical particle in a homogeneous medium, the model we have developed is applicable to any value of the governing parameters x and ρ . Depending upon the values of x and ρ , however, it may be possible to obtain asymptotic expressions which are faster to calculate and easier to interpret. For example, when the index of refraction ratio is close to unity ($m \approx 1$, as is the case for the data which will be presented in Sects. 4 and 5, it is possible to delineate three regions (van de Hulst 1981). With $x \ll 1$ and $|m|x \ll 1$, Rayleigh scattering is obtained. Conversely, when $x \gg 1$ and $\rho/2$ is large compared with unity, the scattering may be separated into a contribution which arises from diffraction plus a term which may be determined from geometrical optics; in this case, the diffraction term is much narrower and more intense. In Sects. 4 and 5, data will be presented for which $x \gg 1$ and $\rho/2$ is not too much greater than unity. In this regime, the contribution from refraction intensifies and becomes more forward peaked (see, e.g., Fig. 2a). The resulting complicated interference in this regime between the diffracted and transmitted light produces a “set of queer scattering diagrams” (van de Hulst 1981). As an example of the spatial variations in the scattering pattern which may arise in this regime, Fig. 4 illustrates the scattered intensity, predicted by far-field Mie calculations, which would be measured on

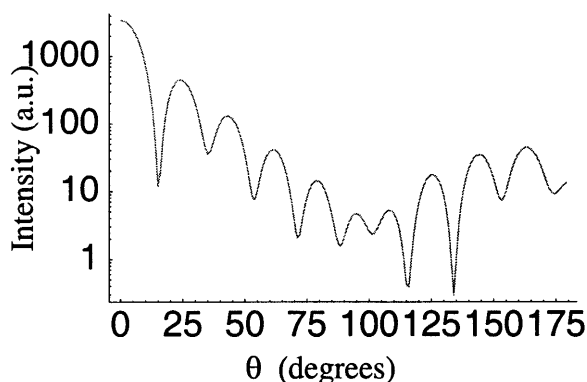


Fig. 4. Scattered intensity (a.u.) as a function of angle from a sphere with $m = 1.33 + i \times 10^{-8}i$ and $x = 10$. The forward direction is at $\theta = 0$

the fluid side of the interface for a slightly absorptive water droplet in air ($x = 10$ and $n_p = 1.33 + i \times 10^{-8}i$) as a function of the observation angle, θ . By definition, $\theta = 0$ is in the forward scattering angle.

In order to determine the scattering as accurately as possible, the model uses Mie calculations to obtain the scattering for any value of the governing parameters x and ρ . Even more importantly, the exact solution is employed because a rigorous analysis of the scattering (Ovryn and Izen 2000) has shown that applying the usual far field approximations can lead to significant error when the particle is close to the interface.

4 Experimental methods

In this section, the details of three experimental procedures are described. Because Mie’s exact solution was formulated assuming that plane wave illumination is incident on a spherical particle, the first experiment was performed in order to verify that a microscope’s Köhler illuminator produces plane wave illumination that has spatial coherence over a circular area at least as large as the cross sectional area of the 7 μm -diameter spheres used in the experiment. In the second experiment, designed to verify that the model could be used to accurately predict the position of a particle along the optical axis, the scattering was measured from a single particle at various locations along the optical axis, and the results were correlated with model predictions. The third experiment applied the technique to spatially resolve the variation in the mean velocity component across a thin channel, i.e., to reconstruct the shear profile in a parabolic flow.

4.1 Plane wave illumination in a microscope

According to theory, the degree of coherence of the illumination increases as the diameter of the aperture stop on a Köhler illuminator decreases (Born and Wolf 1980). To verify this prediction, a microscope (Zeiss, Jenapol Interphako) equipped with a 25 \times /0.5 NA long working distance objective was used in transmitted light to observe the diffraction pattern from a 6- μm -diameter circular hole (Geller Microanalytical, Inc., Model MRS-3). The illuminating wavefront was produced using the microscope’s Köhler white light source with a notch filter; the wavelength of the illumination was measured to be $\lambda = 0.525 \mu\text{m} \pm 85 \text{ nm}$. The microscope was equipped with a high-density digital CCD array (Photometrics PXL 1400) which has 1317×1035 pixels. The dynamic range of the CCD was 12 bits and the array was cooled to minus 25 $^\circ\text{C}$.

4.2 Spatially resolved scattering from spheres inside a microfluidic flow cell observed with a microscope

To measure the scattering from spheres in a fluid medium, a thin channel was produced from two glass microscope slides (thickness 1.25 mm, $n = 1.5$) separated by a spacer and held in a frame. The dimensions of the cell were 6 mm \times 48 mm \times 0.315 mm corresponding to the directions of the x , y , and z axes, as defined in Fig. 1. The cell was filled from one side through an inlet with immersion

liquid (Cargille, Inc., index of refraction $n_f = 1.495$, density $\rho_f = 0.88 \text{ g/cm}^3$, and viscosity $\mu = 27 \text{ cps}$). Spherical polystyrene particles (Duke Scientific Corp., cat: #252) with diameter $2a = 7.0 \pm 0.2 \text{ }\mu\text{m}$ and density $\rho_p = 1.05 \text{ g/cm}^3$ were dehydrated from the manufacturer's solution, mixed with the immersion liquid and then introduced into the flow cell. The index of refraction of the particles at the illumination wavelength, determined from the dispersion curves for polystyrene, was estimated to be $n_p = 1.57$.

Data were acquired in a two-step process. The first step was to identify a single particle that was adhered to the top wall of the glass cell and then to center it along the optical axis. After a brief shear was introduced into the fluid (by rapidly opening the exit valve), the particle was dislodged from the top slide and began to fall downward (toward the illumination source). After the cessation of the shear, the particle's mean transverse displacement was nearly imperceptible. The particle's settling velocity was then measured by manually changing the focus of the microscope so as to maintain a fixed image of the particle. The measured velocity ($10.2 \pm 1.6 \text{ }\mu\text{m/min}$) agreed with the Stokes velocity predicted from the density difference and particle radius ($10.1 \text{ }\mu\text{m/min}$).

In the second step, the focus of the microscope was kept fixed slightly below the midpoint of the channel ($100 \pm 5 \text{ }\mu\text{m}$ above the interior of the bottom slide). Another sole particle was similarly positioned along the optical axis and then dislodged from the top slide. Without changing the focus of the microscope, 80 images were acquired at 15-s intervals. Using the previously calculated velocity, an estimate of the particle's location along the OA was determined for each of the images.

To compare the measured scattering from a single particle with the scattering predicted from the model, the intensity along a single row of pixels through the center of the particle was determined from each of the 80 images. Although the transverse displacement of the particle was small, care was taken to insure that the row of pixels was obtained through the centroid of each image. Because the model assumes that the amplitude of the incident plane wave was unity, the intensity at every pixel of the acquired data was normalized with respect to the intensity that was determined from an image obtained in the absence of the particle. This background intensity is also equal to the intensity far from the center of the particle (provided no other particle is present at that location). A dark current image was also subtracted from each of the acquired data sets.

4.3 Measurement of three-dimensional velocities in a microscopic field-of-view

To measure the three components of a particle's velocity in a seeded flow, the following steps had to be implemented: (1) acquire the data; (2) separate the scattering of individual particles; (3) determine the transverse velocity by tracking the centroid of the centro-symmetric scattering patterns; and (4) determine the axial velocity by comparing the measured and numerically calculated intensity. To determine the axial location, both a trained neural network (Ovryn et al. 1995) and correlative schemes (Ovryn et al. 1998) have been investigated.

A syringe pump (Sage Instruments, Inc.) with a 1-ml gas syringe was used to establish a uniform flow in the thin channel. The flow rate was chosen so that the maximum transverse velocity of the flow did not introduce discernible blur of the scattering patterns. Similarly, the seeding density was chosen so that fewer than 10 particles were observed in a single frame. Data were acquired from a region near the center of the cell (with respect to the x and y axes) at 2 frames/s using an integration time of 0.01 s.

5 Results

In this section, results are presented which demonstrate that uniform, plane wave illumination was achieved using the Köhler illuminator in the microscope. Additionally, the variations in the scattering patterns with respect to changes in position along the OA are presented initially in a qualitative manner and subsequently in a quantitative form. Finally, the results from a measurement of the Poiseuille flow in a thin channel are presented.

5.1 Plane wave illumination in a microscope

Figure 5 shows an image of the circular hole obtained before and after closing the illuminating aperture stop from 8 to 2 mm. Figure 5a demonstrates that, with the

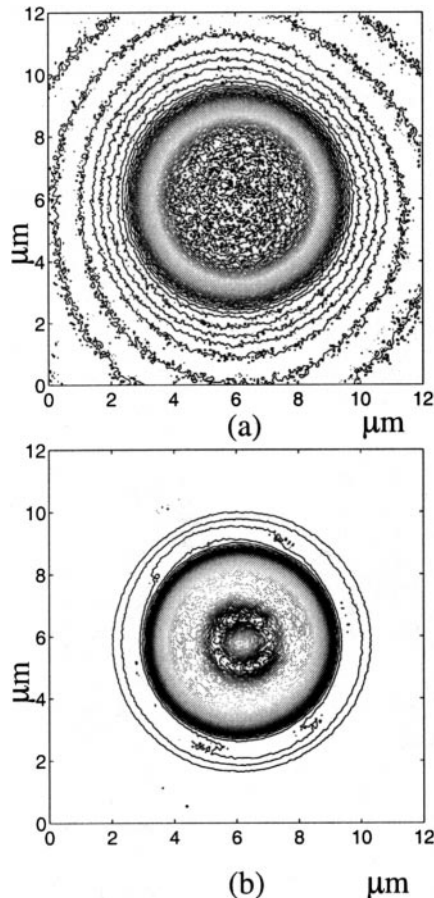


Fig. 5a, b. Measured intensity from a 6- μm circular disk when the aperture stop of the Köhler illuminator was set to: a 8 mm; b 2 mm. Diffraction is observed in b but not a

aperture wide open, the intensity varies uniformly across the pinhole. With the aperture reduced to 2 mm (Fig. 5b), the light is diffracted by the hole and an Airy pattern may be observed (Born and Wolf 1980).

5.2 Qualitative axial and transverse variation in the measured intensity

Figure 6a shows the measured intensity from two essentially identical, 7- μm -diameter spheres. Because it was known a priori that the two spheres have the same size, the variations observed in Fig. 6a were attributed to the difference in axial position of the spheres. The intensity along a row of pixels through the center of each of the patterns in Fig. 6a is shown in Fig. 6b and c. In Fig. 6b and c, the distance from the center of the sphere has been normalized to the sphere's radius, a and the intensity is displayed in the number of measured bits.

It can be observed from Fig. 6 that the variation in intensity at distances from the center of the particle beyond about $r = 3a$ is small. Focusing of the transmitted light (see Fig. 2) causes the bright spot in the center of the particles (Fig. 6c). This strongly peaked forward scattering is expected for particles with large size parameters.

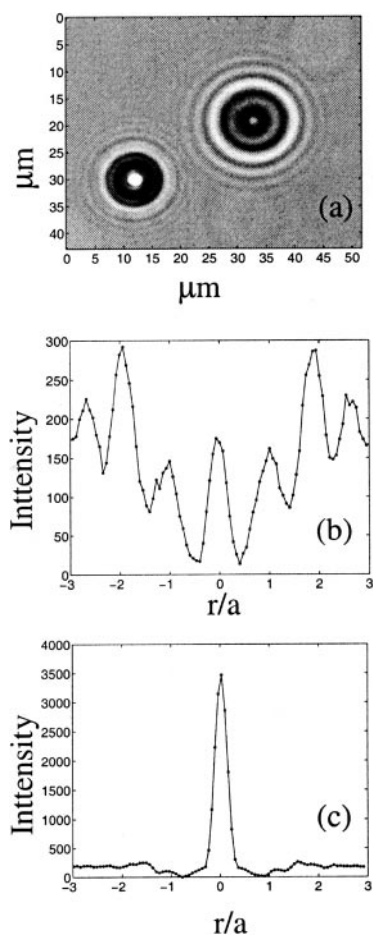


Fig. 6a-c. High-density CCD image of the scattering of two 7.0- μm -diameter polystyrene spheres at different positions along the optical axis. Also shown is the intensity along a line through the center of each sphere. The transverse distance along each scattering pattern is normalized with respect to the particle radius, a

5.3 Comparison of the measured and numerically predicted intensity

Figure 7a represents a montage of the normalized intensities from each of the row of pixels for all of the images. The distance along the optical axis, δ , and the transverse distance are normalized with respect to the particle's radius. The data in Fig. 7a were not averaged in any manner. Figure 7b represents the numerically calculated normalized intensities assuming unpolarized illumination. Because the numerical data set may be calculated at any arbitrary location, δ , along the optical axis, this data set is denser, representing the scattering at intervals of 1.0 μm inside the fluid. It can be observed that the scattering is highly asymmetric with respect to the image obtained at $\delta = 0$.

A quantitative comparison of the measured data and numerically computed scattering at six axial locations is shown in Fig. 8. The six axial locations, chosen to be approximately symmetric with respect to $\delta = 0$ were: -25.7, -6.1, -2.5, +4.0, +14.90 and +22.1 μm (Fig. 8a-f, respectively). The data in Fig. 8 indicate good agreement between the measured and numerically calculated data. At any axial location, the measured data are nearly symmetric with respect to the center of the particle, however, small variations due to random noise may be observed.

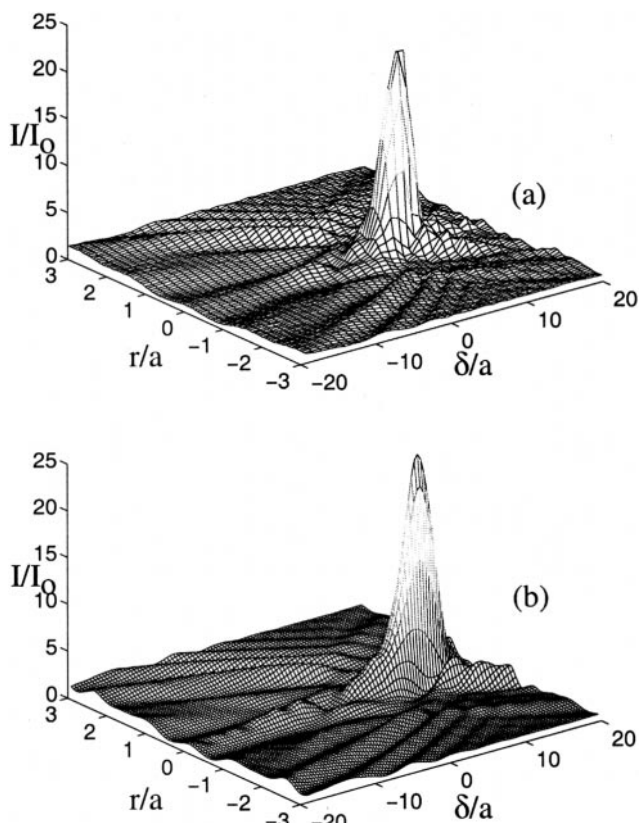


Fig. 7a, b. Measured intensity from a sphere: a at various axial positions along the optical axis; b numerically calculated intensity. The intensity is normalized with respect to the background intensity, I_0 , and the axial distance, δ , is normalized with respect to the particle's radius. Both data sets represent a montage of the intensity along a single line through the center of the particle

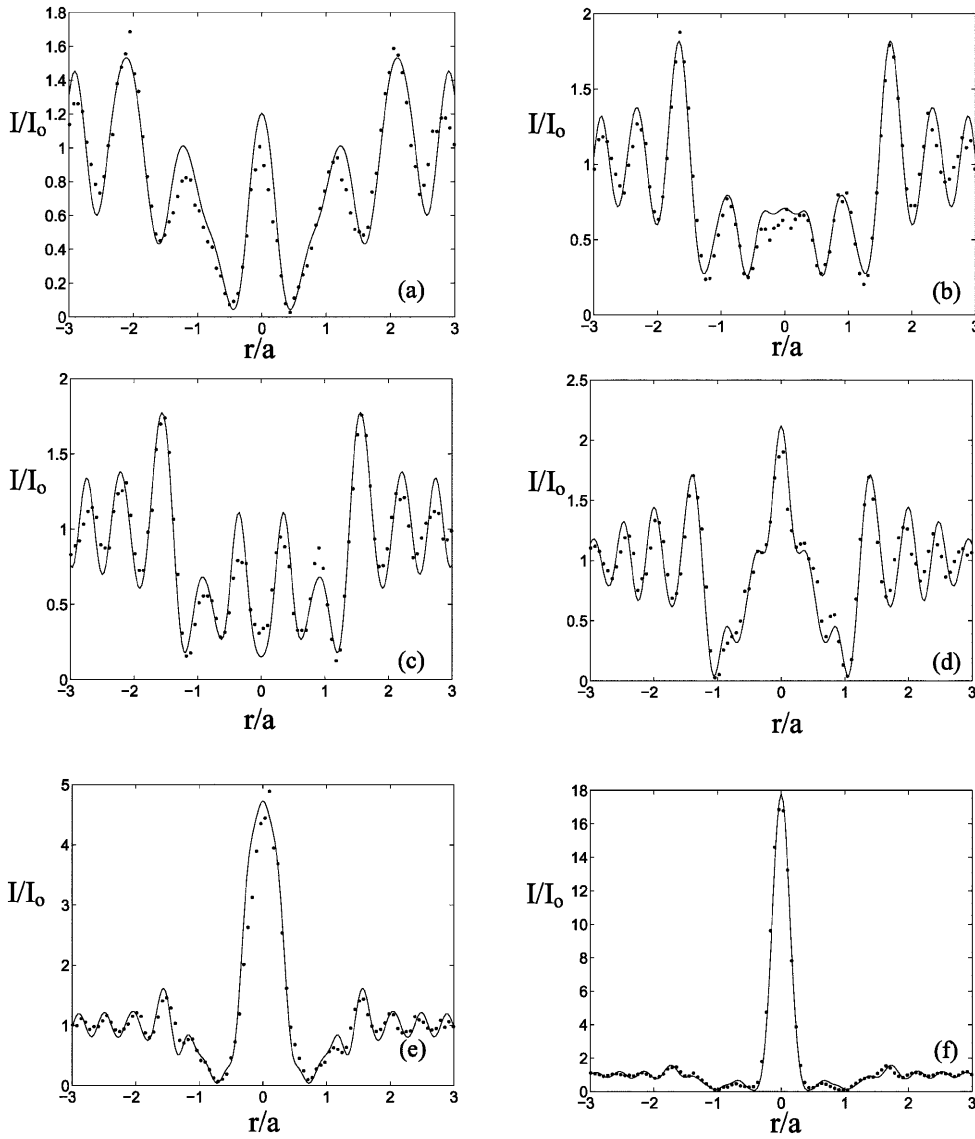


Fig. 8a-f. Comparison between measured (dotted line) and numerically predicted intensity as a function of transverse position on the detector plane. The distances δ were: -25.7 , -6.1 , -2.5 , $+4.0$, $+14.9$ and $+22.1$ μm (a-f, respectively)

In order to obtain agreement between the measured and numerically calculated data (Fig. 8), the values for the experimental parameters had to be adjusted from their initially assumed values. The initial estimates for these values were: $n_p = 1.57$; $n_f = 1.495$; $a = 3.5$ μm ; $\lambda = 0.525$ μm . Using these values, the parameters m , x , and half of the phase shift, $\rho/2$, were 1.0517, 62.62, and 3.14159, respectively (the value near π is an interesting coincidence). The index of refraction, particle radius and wavelength used in the fit, however, were $n_p = 1.585$, $a = 3.65$ μm , and $\lambda = 0.51$ μm .

5.4 Effect of transverse and axial particle displacements on the scattering

Because the model calculations fit the experimentally measured data quite well, it is possible to simulate, rather than measure, the effect of either a transverse or axial displacement of the particle on the scattering patterns. For example, Fig. 9 demonstrates the effect of a relative transverse shift of one pixel between the collected scattering and the calculated scattering pattern for the data represented in Fig. 8f. The data in Fig. 9 represent the

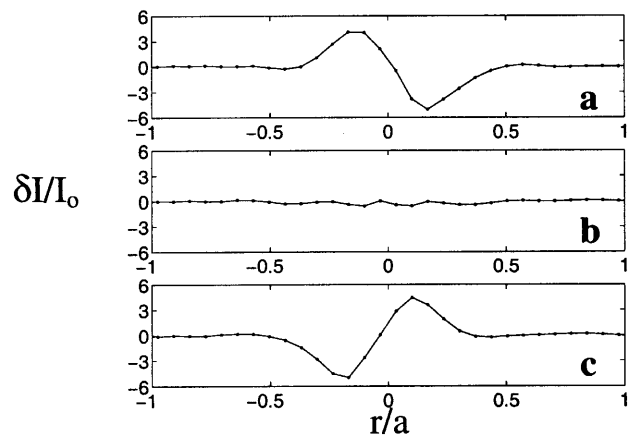


Fig. 9a-c. Difference between the theoretical and experimental data both with (a and c) and without (b) a relative transverse shift for the data at $\delta = 22.1$ μm . The relative shifts were one pixel which corresponds to ± 110 nm. δI means change in I

difference between the experimentally measured and calculated data for a relative single pixel left shift (Fig. 9a), no shift (Fig. 9b) and a right shift (Fig. 9c). A single pixel

shift represents a relative displacement of approximately 110 nm. Similarly, Fig. 10 represents the effect of a two-pixel shift for the data in Fig. 8a.

Although the effect of a displacement of the axial position of a particle has been shown for discrete locations in Fig. 8, Fig. 11 shows the continuous spatial variation of the intensity. It may be observed that there are certain positions along the optical axis, corresponding to extrema of the spatial derivative of the intensity, where the sensitivity to an axial displacement would be greatest. Using the data in Fig. 8f (which were acquired near an extremum of the derivative), it is possible to simulate the effect of a relative axial change by subtracting the data from theoretically predicted data sets which correspond to several values of δ . For example, the difference between the data in Fig. 8f and the calculated data set at the correct axial location ($\delta = 22.7 \mu\text{m}$) was shown in Fig. 9b. Figure 12 shows the difference between the data and a calculated data set shifted by $\pm 400 \text{ nm}$ with respect to the correct axial location. This shift value was chosen as an example that leads to a change in the normalized intensity, which is clearly greater (without averaging the data) than the random noise in the data.

5.5 Simulated effect of imaging with a low numerical aperture objective

Using the model, it is also possible to simulate the characteristics of the scattering patterns as if they had been

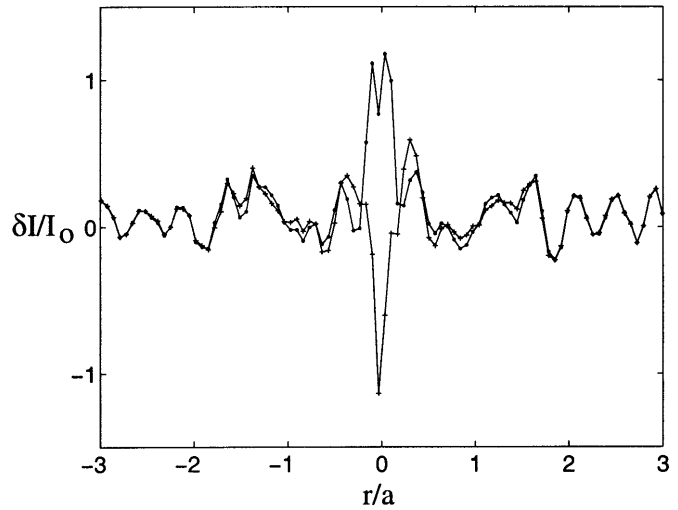


Fig. 12. Difference between the theoretical and experimental data with a relative axial shift of $\pm 400 \text{ nm}$ from the axial location of $\delta = 22.1 \mu\text{m}$

measured with a lower numerical aperture microscope objective. Figure 13 shows the simulated effect of imaging the scattering patterns with an objective lens with $\text{NA} = 0.14$ instead of the $\text{NA} = 0.5$ lens used in the experiments. As expected, it can be observed that the lower-NA lens low-pass filters the detailed structure of the scattering pattern.

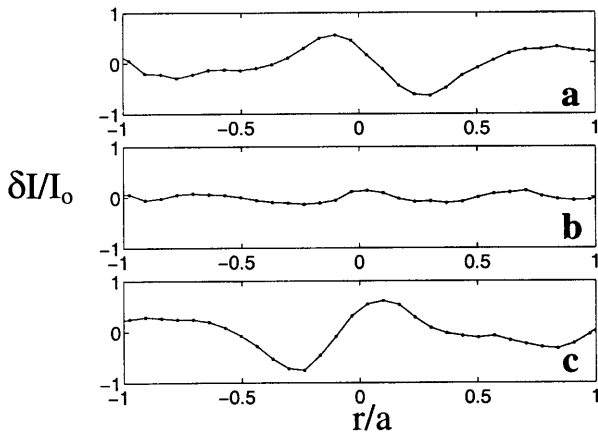


Fig. 10a-c. Difference between the theoretical and experimental data both with (a and c) and without (b) a relative transverse shift for the data at $\delta = -25.7 \mu\text{m}$. The relative shifts were two pixels which corresponds to $\pm 220 \text{ nm}$

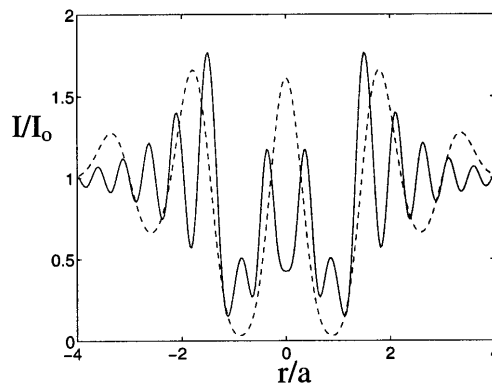


Fig. 13. Simulated effect of imaging with a microscope objective with $\text{NA} = 0.14$ compared with a $\text{NA} = 0.5$ lens (solid curve). With the lower NA objective, the detailed structure is lost due to low pass filtering

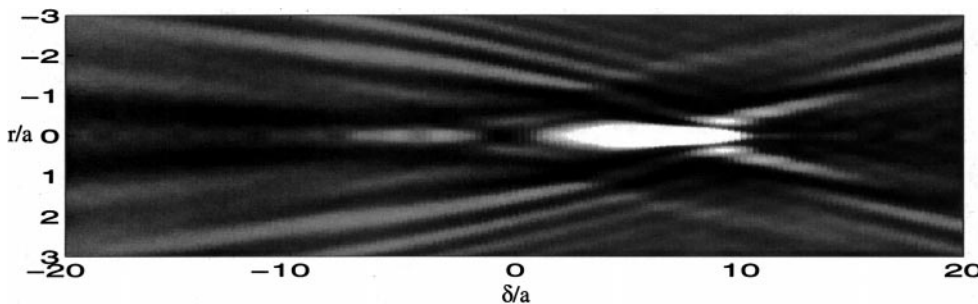


Fig. 11. Numerically computed axial and transverse variation in the scattering from a $7.0\text{-}\mu\text{m}$ sphere. As in Fig. 7, the intensity is normalized with respect to the background intensity, I_0 , and the axial distance, δ , is normalized with respect to the particle's radius

5.6

Measurement of Poiseuille flow in a thin channel

Figure 14 shows four typical sequential images of particles moving within the 315 μm channel; within each frame, the

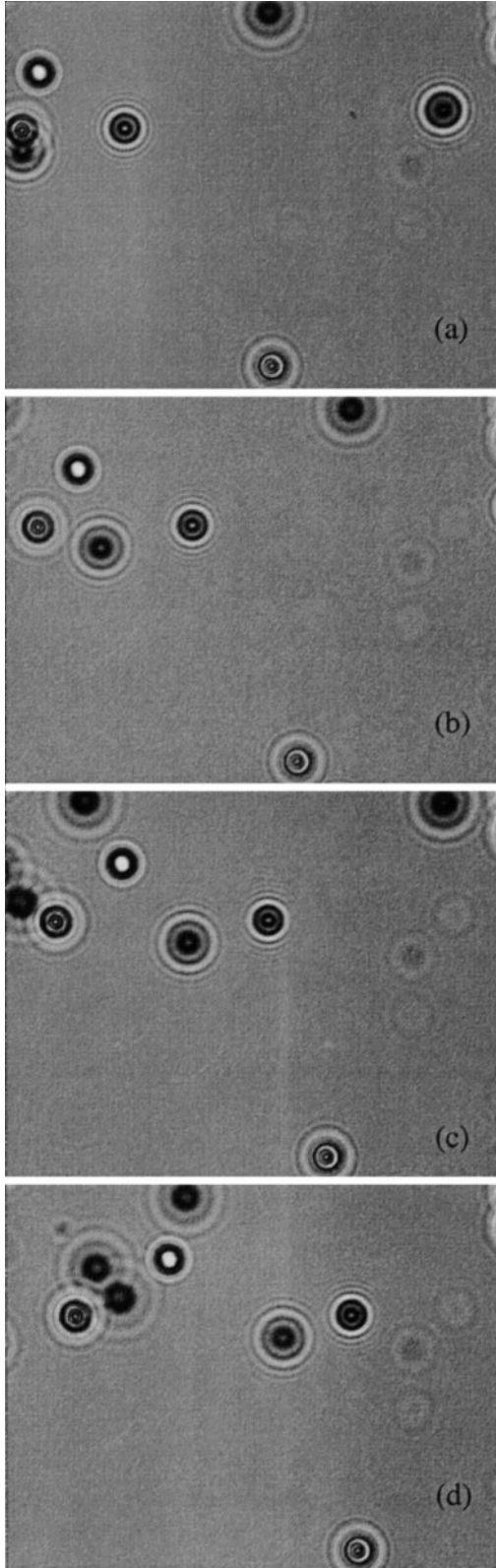


Fig. 14a-d. Four images acquired sequentially at 2 frames/s (from top to bottom) when the flow is from left to right

flow is from left to right. From these images, acquired sequentially (Fig. 14a-d), it is apparent that the particles are in different planes. For example, two particles are observed to overlap in Fig. 14a and then to separate in the subsequent frame (Fig. 14b). The different transverse velocities of particles may also be observed. To determine the transverse velocity of a particle, the centroid was determined and tracked as a function of time. Figure 15 shows an example of the centroid determination from one of the spheres shown in Fig. 6.

Figure 16 shows the transverse velocity at specific axial locations determined by manually tracking 22 randomly positioned particles for the 21 acquired frames (a schematic of the flow channel is also shown). Because of particle settling prior to taking the velocity data, the velocity could not be determined in the region above about 200 μm . As indicated in Fig. 16, within the measured FOV, a variation in the velocity was observed parallel to the flow direction (y axis, Fig. 1), but there was no appreciable flow transverse to the mean flow direction (x axis, Fig. 1).

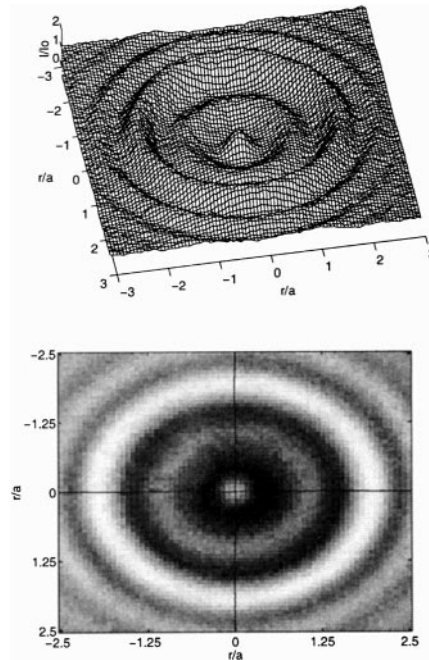


Fig. 15. Centroid determination (bottom contour plot) from the centro-symmetric scattering from one of the particles from Fig. 6

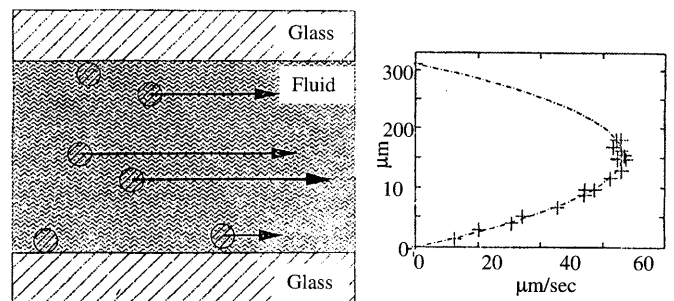


Fig. 16. Parabolic velocity profile determined across the thin channel

Discussion and conclusions

The method developed for determining the three-dimensional position of a spherical particle is based upon resolving the detailed spatial variations in the scattering pattern. This approach uses considerably more information to locate the particle than methods which rely upon the measurement of the changes in the full-width of the intensity at half-maximum (e.g., depth-of-field concepts) (Crocker and Grier 1996). Furthermore, the technique is applicable to any size sphere of arbitrary index of refraction in any homogeneous medium and accounts for the presence of an interface which may be arbitrarily close to the sphere.

Because the model is sensitive to all of the parameters that govern the scattering, as well as the parameters of the optical microscope (including the illumination), multiple parameters, such as size and position, may be determined simultaneously. The trade-off, however, is that the parameter space is quite large and therefore, good initial estimates for these parameters should be obtained in order to facilitate the correlation between model predications and data. In preliminary studies, we have trained a neural network with variations in several of the governing parameters and then requested the network to determine the correct correlation between the data and theoretical results (Ovryn et al. 1995). In this instance, the neural network is essentially a large look-up table. Although this approach has demonstrated that the network can correctly determine the location of a particle along the optical axis by interpolating between training sets, the precise location of the sphere was not always determined accurately.

A representative application of the technique to the determination of the velocity profile across a thin-channel flow has been presented using a monodisperse distribution of spherical tracers. Although the data were acquired with a low noise, slow CCD camera, it would be possible to acquire low noise data significantly faster using newer technology. With sufficient frame rate, the observer can clearly see particles moving in different planes which are transverse to the optical axis (Fig. 14). As shown in Fig. 11, the spatial variations in the scattering patterns differ from the background over a range, δ , of at least 30 particle radii. Therefore, the scattering patterns from spheres at different axial locations may overlap (Fig. 14). To reduce image overlap, the seeding density has intentionally been kept low; of course, the seeding density must be high enough to sample the essential spatial variations in the flow. It would also be possible to probe the spatial variations in the flow by using spheres with distinctly different diameters.

It is difficult to precisely determine the maximum tolerable seeding density, because the errors at high densities depend significantly upon the robustness of the algorithm which is employed for the initial stage of the image processing. For example, in Fig. 14a the column of pixels obtained through the centroid of the two overlapping particles would be quite difficult to separate into two distinct scattering patterns. A row of pixels obtained separately through the centroid of each of the spheres, however, could be used for further processing. In this case,

a correlation between model and data could nevertheless be obtained, but the weak side lobes of the scattering from the two particles would decrease the precision of the fit. Similarly, Fig. 14d shows the overlap of four scattering patterns, two of which are observed to be nearly identical (indicating that they are at the same position along the optical axis). Again, a sophisticated image processor could identify line cuts which are only moderately influenced by the presence of the side lobes of the other patterns. Furthermore, a shear flow should tend to separate the overlapping particles and therefore, they may become clearly distinct in subsequent frames.

Alternatively, it would be possible to increase the acceptable seeding density by augmenting the model to account for the coherent superposition of the electromagnetic fields from the forward scattering of several particles (Boren and Huffman 1983). In essence, this approach would lead to a new resolution criteria, analogous to Rayleigh's two-point resolution criterion (Born and Wolf 1980), but extended to a three-dimensional vector separation between spheres. Unlike Rayleigh's criterion, which states that two apertures may be distinguished when the intensity measured along a line between the two centers of the apertures dips by at least 26%, the three-dimensional analogue would use considerably more information about the scattering and image formation process and therefore quite small separations could be determined. The interpretation of the experimental data has also been simplified by assuring that the maximum flow velocity was chosen to be small enough such that blurring of the scattering patterns during the acquisition is imperceptible; for very fast flows, the validity of this assumption requires both a bright light source and a fast detector. If these assumptions are not valid, it would be necessary to model the effect of the sphere's motion on the blurring of the scattering patterns.

The data in Figs. 9, 10 and 12 show examples of how the model may be applied to determine small axial and transverse displacements. Figure 12 demonstrates that axial displacements of ± 400 nm produce a change in the intensity which is significantly greater than the noise. Because this displacement was measured at an axial location of the sphere where the rate of change of the intensity with respect to distance was nearly maximum (Fig. 11), this displacement is close to the best obtainable for any location of the sphere. This is a conservative estimate, however, because it may be observed that smaller displacements can produce statistically significant changes in the measured intensity. Because the data are radially symmetric, averaging radial line cuts may be used to reduce the noise and therefore improve the displacement resolution. Analogously, the magnitude of the change in the measured intensity caused by a transverse displacement (Figs. 9 and 10) also depends upon the axial position of the sphere, i.e., the sensitivity is much greater when $\delta = 22.10$ than when $\delta = -25.70$.

Although the model has been developed primarily to predict the image using a high numerical aperture objective assuming plane wave illumination of a spherical particle and a collection cone centered along the forward scattered direction, the model could be extended to

situations where these assumptions are not valid. For example, the model may be extended to measure the scattering at other angles (including reflected light). It would also be possible to relax the assumption of plane wave illumination to include incident Gaussian beams with finite coherence and off-axis imaging (Schaub et al. 1989, 1991; Ren et al. 1996; Pralle et al. 1999). Although laser beam illumination is commonly used in many important applications (e.g., laser tweezers), illumination with a Köhler source simplifies the model considerably and reduces the speckle noise in the images.

References

- Barber PW; Hill SC** (1990) Light scattering by particles: computational methods. World Scientific, New Jersey
- Barnhart DH; Adrian RJ; Papen GC** (1994) Phase-conjugate holographic system for high-resolution particle-image velocimetry. *Appl Opt* 33: 7159–7170
- Boren CF; Huffman DR** (1983) Absorption and scattering of light by small particles. Wiley, New York
- Born M; Wolf E** (1980) Principles of optics, 6th edn. Pergamon, New York
- Crocker JC; Grier DG** (1996) Methods of digital video microscopy for colloidal studies. *J Colloid Interface Sci* 179: 298–310
- Denk W; Webb WW** (1990) Optical measurement of picometer displacements of transparent microscopic objects. *Appl Opt* 29: 2382–2390
- Dufresne ER; Squires TM; Brenner MP; Grier DG** (2000) Hydrodynamic coupling of two brownian spheres to a planar surface. *Phys Rev Lett* (in press)
- Fabry EP** (1998) 3D holographic PIV with a forward-scattering laser light sheet and stereoscopic analysis. *Exp Fluids* 24: 39–46
- Gittes F; Schnurr B; Olmsted PD; MacKintosh FC; Schmidt CF** (1997) Microscopic viscoelasticity: shear moduli of soft materials determined from thermal fluctuations. *Phys Rev Lett* 79: 3286–3289
- Hinsch KD** (1995) Three-dimensional particle velocimetry. *Meas Sci Technol* 6: 742–753
- Imai Y; Tanaka K** (1999) Direct velocity sensing of flow distribution based on low-coherence interferometry. *J Opt Soc Am A* 16: 2007–2012
- Izen S; Ovrzyn B** (1998) Imaging spheres with general incident wavefronts using a dipole decomposition. *SPIE J* 3261: 7–16
- Kepler GM; Fraden S** (1994) Video microscopy study of the potential energy of a colloidal particle confined between two plates. *Langmuir* 10: 2501
- Khaydarov JD; Ovrzyn B** (1996) Measurement of three dimensional velocity profiles in a thin channel flow using forward scattering particle image velocimetry (FSPIV). In: Proceedings, 1996 ASME Fluids Engineering Division Summer Meeting 239(4): 403–408
- Mason TG; Ganesan K; van Zanten JH; Wirtz D; Kuo SC** (1997) Particle tracking microrheology of complex fluids. *Phys Rev Lett* 79: 3282–3285
- Meiners JC; Quake SR** (1999) Direct measurement of hydrodynamic cross correlations between two particles in an external potential. *Phys Rev Lett* 82: 2211–2214
- Meng H; Hussain F** (1991) Holographic particle velocimetry: a 3D measurement technique for vortex interactions, coherent structures and turbulence. *Fluid Dyn Res* 8: 33–52
- Ovrzyn B; Hallinan K; Das K** (1998) Quantitative, three-dimensional flow, in a microscopic field-of-view. In Proceedings, 1998 ASME Fluids Engineering Division Summer Meeting FEDSM98 5268: 1–7
- Ovrzyn B; Hovenac EA** (1994) Coherent forward scattering particle image velocimetry: application of Poisson's spot for velocity measurements in fluids. *SPIE J* 2005: 338–348
- Ovrzyn B; Izen S** (2000) Imaging of transparent spheres through a planar interface using high-numerical aperture optical microscope. *J Opt Soc Am A* 17: 1202–1213
- Ovrzyn B; Khaydarov JD** (1997) Forward scattering particle image velocimetry (FSPIV): application of Mie and imaging theory to measure 3D velocities in microscopic flows using partially coherent illumination and high aperture optics. *SPIE J* 2984: 243–254
- Ovrzyn B; Wright T; Khaydarov JD** (1995) Measurement of three-dimensional velocity profiles using forward scattering particle image velocimetry (FSPIV) and neural net pattern recognition. *SPIE J* 2546: 112–124
- Pralle A; Prummer M; Florin EL; Stelzer EHK; Horber JKH** (1999) Three-dimensional high resolution particle tracking for optical tweezers by forward scattered light. *Microsc Res Technol* 44: 378–386
- Prasad AK; Adrian AJ** (1993) Stereoscopic particle image velocimetry applied to liquid flows. *Exp Fluids* 15: 49–60
- Ren KF; Lebrun D; Özkul C; Gouesbet G; Gréhan G** (1996) On the measurement of particles by imaging methods: theoretical and experimental aspects. Part Part Syst Charact 13: 156–164
- Santiago JG; Wereley ST; Meinhart CD; Beebe DJ; Adrian RJ** (1998) A particle image velocimetry system for microfluidics. *Exp Fluids* 25: 316–319
- Schaub SA; Alexander DR; Barton JP** (1989) Theoretical model for the image formed by a spherical particle in a coherent imaging system: comparison with to experiment. *Opt Eng* 28: 565–571
- Schaub SA; Alexander DR; Barton JP** (1991) Theoretical model of laser imaging of small aerosols: application to aerosol sizing. *Appl Opt* 30: 4777–4784
- Svoboda K; Schmidt C; Schnapp BJ; Block SM** (1993) Direct observation of kinesin stepping by optical trapping interferometry. *Nature* 365: 721–727
- van de Hulst HC** (1981) Light scattering by small particles. Dover, New York
- Visscher K; Block SM** (1998) Versatile optical traps with feedback control. *Methods Enzymol* 298: 460–489
- Wang X; Milner TE; Chen Z; Nelson JS** (1997) Measurement of fluid-flow-velocity profile in turbid media by the use of optical Doppler tomography. *Appl Opt* 36: 144–149
- Wernet MP** (1996) Stereo viewing 3-component, planar PIV utilizing fuzzy inference. NASA Technical Memorandum 107235
- Wernet MP; Pline A** (1993) Particle displacement tracking technique and the Cramer-Rao lower bound error in centroid estimates from CCD imagery. *Exp Fluids* 15: 295–307
- Willert CE; Gharib M** (1991) Digital particle image velocimetry. *Exp Fluids* 10: 181–193
- Yazdanfar S; Kulkarni MD; Izatt JA** (1997) High resolution imaging of in vivo cardiac dynamics using color Doppler optical coherence tomography. *Opt Ex* 13: 424–431